



Perylene-3,4,9,10-tetracarboxylic acid accelerated light-driven water oxidation on ultrathin indium oxide porous sheets



Ruijin Zheng^{a,b,c}, Miao Zhang^{b,c}, Xun Sun^{b,c}, Ruiping Chen^d, Xuan Sun^{a,*}

^a Key Laboratory of Colloid and Interface Chemistry & Key Laboratory of Special Aggregated Materials, Shandong University, Ministry of Education, Jinan 250100, PR China

^b State Key Laboratory of Crystal Materials, Shandong University, Jinan 250100, PR China

^c Key Laboratory of Functional Crystal Materials and Device (Shandong University), Ministry of Education, Jinan 250100, PR China

^d State Key Lab of Structural Chemistry Fujian Institute of Research on the Structure of Matter, Chinese Academy of Sciences Fuzhou, 350002, PR China

ARTICLE INFO

Keywords:

Organic/inorganic nanocomposites
Perylene-3,4,9,10-tetracarboxylic acid
Oxygen evolution reaction
Proton-coupled electron transfer

ABSTRACT

Engineering the organic/inorganic nanocomposites by taking advantage of the high electrical conductivity of the inorganic semiconductors and the structure flexibility of the organic semiconductors (OSCs) provides chances to understand the structural and electronic contributions that give rise to increased activities, which is the imperious demand for methodical design of next-generation of oxygen evolution photocatalysts. Herein, perylene-3,4,9,10-tetracarboxylic acid (PTCAD) bonded porous In_2O_3 nanosheets, PTCAD/ In_2O_3 NSs, were fabricated to elucidate the performance of OSCs in light harvesting and charge separation toward photo-driven oxygen evolution reaction (OER). PTCAD coupled strongly to the conduction band (CB) of In_2O_3 NS and type-II energy alignment was constructed between these two organic-inorganic components. Consequently, upon excitation, electrons injected smoothly from PTCAD to In_2O_3 NS, leaving holes behind to perform water oxidation, which results in accelerated charge separation and transportation. Associated with the large specific area, high-speed electron transmission channels, abundant oxygen vacancies and active sites provided by the In_2O_3 NS, the PTCAD/ In_2O_3 composites demonstrated highly reduced band gap (BG), boosted and stable photocurrent, as well as largely reduced overpotential, suggesting promises for broadband-light-triggered OER. In addition to the synergistic effects in promoting charge separation and inhibiting electron-hole recombination, the π -conjugated molecule, PTCAD, played a role of manipulating the lattice plane of the In_2O_3 nanostructure without disturbing its porous 2D structure, providing another potential approach for enhancement of catalytic activity by regulating the crystal faces. Importantly, water oxidation over PTCAD/ In_2O_3 NSs is indeed a proton-coupled electron transfer (PCET) processes, a key process for charge separation and water oxidation, which is significantly promoted by PTCAD. Ultimately, the photo-catalytic oxygen evolution yield enhanced greatly at the presence of PTCAD, indicating that our findings may provide clues for development of organic/inorganic hybrid semiconducting photocatalysts for solar fuels generation.

1. Introduction

Photocatalytic water splitting is accepted as the one effective way to tackle environmental pollution and energy crisis. Broadband-light-induced charge separation and directional charge transport are the most relevant factors in determining the efficiency of photoelectrochemical water splitting. Specifically, for oxygen evolution reaction (OER), the half reaction of water splitting, due to the nature of a four-electron/four-proton process, it is sluggish and is the rate-determining step of water splitting, which typically requires a much higher overpotential to drive the redox reaction [1,2]. Since the dramatic discovery on photo-

evolution of H_2 and O_2 from a TiO_2 electrode of Fujishima and Honda [3], more significant findings have been reported [4–7], leading to the booming development of the semiconductor photocatalysts for light-triggered water splitting. However, most OER available photocatalysts reported thus far are inorganic semiconductors baring large bandgaps (BGs) and deep valence band maximum (VBM) with respect to the water oxidation (WO) potential, therefore broadband-light is not sufficiently used and a substantial overpotential is still necessary, resulting in inefficiency in WO. In addition, fast recombination of the photo-generated charges anterior to WO remains the obstacle for an efficient photocatalysts. Over the past few decades, targeted on addressing the

* Corresponding author.

E-mail address: sunxuan@sdu.edu.cn (X. Sun).

above issues, a great deal of inorganic semiconductor-based systems for photocatalytic WO have been developed, and photocatalytic efficiency have been improved by strategies including anion doping [8,9], transition metal doping [10,11], and heterostructured photocatalysts [12–14]. Semiconductor composites comprising different materials or phases are effective in facilitating charge separation and vectoring charge carrier transfer, which substantially improve photocatalytic and photoelectrochemical efficiency [15].

Organic molecules that are promising for low cost, earth-abundance, and especially flexible structural tenability have long been underestimated for photocatalysis. Molecules with high and broad absorption in visible region have been employed as antenna to sensitize the catalyst active center in artificial photosynthesis [16]. Nevertheless, organic molecules on mediating charge transport in photocatalysis is barely acknowledged. Trifluoroacetic acid (TFA) was proposed as molecular co-catalyst to accelerate the hole transfer kinetics by virtue of the reversible redox couple $\text{TFA}^{\bullet}/\text{TFA}^-$, which effectively accelerated photocatalytic H_2 production [17]. Actually, recent studies have evidenced that the interface charge (electron or hole) transfer may associate with proton transfer, namely proton-coupled electron transfer (PCET), by which Tyr-His pair participates the catalyzed water splitting in Photosystem II [18]. For oleylamine (OAm) layer capped Co_3O_4 , PCET process was demonstrated to greatly facilitate the oxygen evolution reaction, shedding light on methods to improve the OER activities in neutral environment. The development of organic nanoelectronics in recent years has witnessed the importance of organic molecules in charge transport. Perylene-3,4,9,10-tetracarboxylic diimide (PDI) and its derivatives are one of the most excellent n-type OSC, profiting from its outstanding thermal and photo-stability, high molar absorptivity, and high charge carrier mobilities [19–21]. The molecular structure of PDIs can be readily tailored which make them especially interesting for constructing organic-inorganic hybrid semiconductors with matched energy level [22]. These properties have made PDIs attractive materials for fundamental studies on water-splitting applications. Using PDIs as light-harvesting material, DS-PEC architectures have been built based on selected metal oxide (MO_x) semiconductors [23–27]. Low-energy excitation and long-standing charge separation are realized through the inter-component charge transfer. By rational engineering the organic and inorganic semiconductor counterparts, enhancement of the absorption in a wider visible range and separation of the photo-generated charge carriers are prospective.

Indium oxide (In_2O_3) is a well-known n-type semiconductor with excellent conductivity for photoelectric-conversion cells. Particularly attractive is its high stability even in strong acid solutions, which is a hot potato for most reported metal oxide semiconductors used in OER under the circumstance of low pH. Together with the suitable valance band (VB) edge, In_2O_3 shows promise for OER [28]. However, the large BG (ranging from 2.9 to 3.7 eV) [29] make it inefficient in utilizing AM1.5 solar spectrum, and consequently the overall less power conversion efficiency for water splitting [30]. By confinement of oxygen vacancies in ultrathin In_2O_3 porous nanosheets, Xie et al reported that the BG of In_2O_3 was narrowed from the UV to visible regime because of the newly created donor levels endowed by O-vacancies, which also lead to the improved carrier separation efficiency [31]. Considering the virtue of the 2D structured semiconductors, namely the 2D-limited conducting channels that act as carrier pathways for the quick separation of electron-hole pairs, and the large surface area that may provide abundant active sites for surface reactions [32–34], we are intention to fabricate PTCAD functionalized In_2O_3 nanosheets (NS) to get insight into the structural and electronic effects of exerting OSCs on photocatalytic WO. PTCAD/ In_2O_3 NS was fabricated via a rapid and facile method as illustrated in **Scheme 1**. The absorption of the PTCAD/ In_2O_3 NS is broadened into visible region relative to the pristine In_2O_3 NS, as the result of the 2D structures and the contribution from the PTCAD. The photocurrent intensity was markedly enhanced at the presence of PTCDA, especially for the hybrid with 0.5% mol fraction of PTCDA,

indicating the effective inhibition of charge recombination originated from the strong donor-acceptor electron coupling at the $\text{In}_2\text{O}_3/\text{PTCDA}$ interface. The overpotential of the PTCDA/ In_2O_3 hybrids was largely reduced relative to the neat In_2O_3 NS, which manifests the strongly enhanced activity of the electrochemical OER stemming from the synergistic effect between the two components. The PTCAD/ In_2O_3 NS hybrids present a model for enhancing the visible light absorption as well as the charge separation and transportation with the target of effective water splitting, based on the synergistic effects and interfacial energy alignment between the organic and inorganic semiconductors.

2. Experimental section

2.1. Preparation of $\text{In}(\text{OH})_3$ nanosheets

0.6 mmol sodium oleate was initially added into 15 mL H_2O , and then stirring for 15 min to create a surface active and alkaline environment. 0.3 mmol $\text{In}(\text{NO}_3)_3 \cdot 2\text{H}_2\text{O}$ was added into the mixed solution. Stirring until solid aggregates completely dissolved. Then the mixture was transferred into a 20 mL teflon-lined autoclave, sealed and heated at 150 °C for 3 h. The final product was collected by centrifuging the mixture, washed with ethanol and acetone for times, and then dried in vacuum drying oven to get dry solid powder for further characterization.

2.2. Preparation of PTCAD/ $\text{In}(\text{OH})_3$ nanosheets

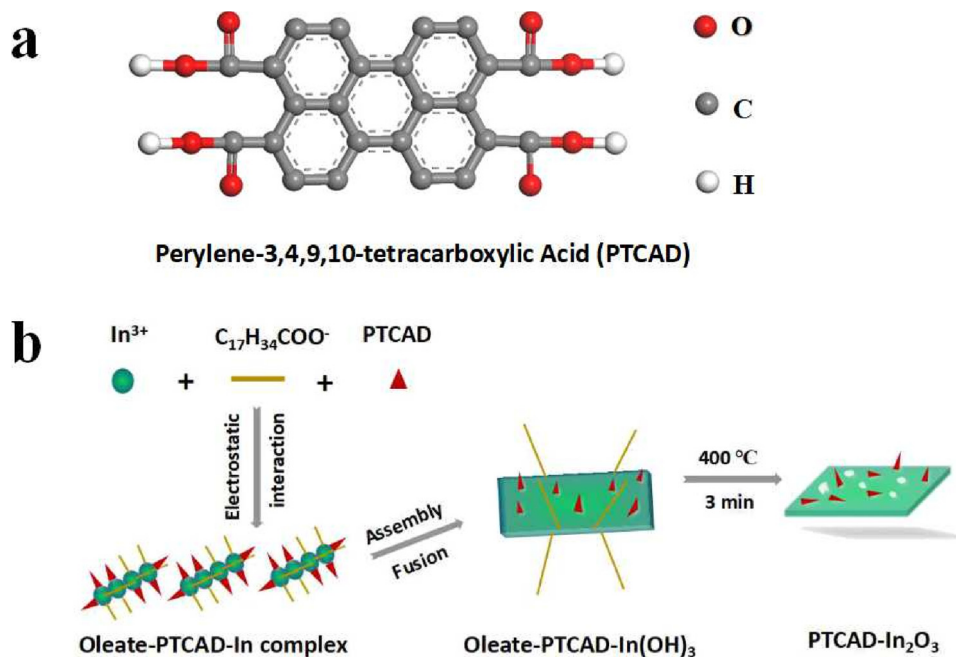
PTCAD/ $\text{In}(\text{OH})_3$ nanosheets were prepared with the same method except that a certain amount of PTCAD is added. Specifically, 16 mg PTCAD dissolved in water and transferred to 50 ml volumetric bottle. 0.6 mmol sodium oleate was initially added into 15 mL H_2O , and then stirring for 15 min to create a surface active and alkaline environment. 0.8 mL, 2 mL, 4 mL PTCAD aqueous solution and 12.8 mg PTCAD powder (0.2%, 0.5%, 1%, 10% molar ratio with $\text{In}(\text{NO}_3)_3 \cdot 2\text{H}_2\text{O}$) were added into mixed solutions, respectively. After stirring for 30 min, 0.3 mmol $\text{In}(\text{NO}_3)_3 \cdot 2\text{H}_2\text{O}$ was added into the mixed solution and stirred until solid aggregates completely dissolved. Then the mixture was transferred into a 20 mL Teflon-lined autoclave, sealed and heated at 150 °C for 3 h. The final product was collected by centrifuging the mixture, washed with ethanol and acetone for several times, and then dried in vacuum drying oven to get dry solid powder for further characterization.

2.3. Preparation of PTCAD- In_2O_3 nanosheets

PTCAD- In_2O_3 and pure In_2O_3 nanosheets were obtained from PTCAD/ $\text{In}(\text{OH})_3$ and pure $\text{In}(\text{OH})_3$ nanosheets by a fast-heating strategy: heat the PTCAD/ $\text{In}(\text{OH})_3$ and pure $\text{In}(\text{OH})_3$ nanosheets at 400 °C for a short time of 3 minutes in air. The obtained powders were collected for further characterization.

2.4. Characterization

The transmission electron microscopy (TEM) images and scanning electron microscopy (SEM) were obtained on a JEM-2010 electron microscope (JEOL, Japan) and a S-4800 field emission SEM (FESEM, Hitachi, Japan), respectively. And the HRTEM was tested by JEM-2100F. The crystal structure was determined by X-ray diffraction at room temperature on HZG41B-PC using Cu $\text{K}\alpha$ radiation ($\lambda = 0.15418 \text{ nm}$). UV-vis diffuse reflection spectra were obtained on a SHIMADZU UV-2405 spectrophotometer. The Brunauer-Emmett-Teller (BET) was measured by Micromeritics ASAP 2020. X-ray photoelectron spectroscopy (XPS) measurements were performed in an ultrahigh vacuum VG ESCALAB 210 electron spectrometer. All the binding energies were referenced to the C 1 s peak at 284.8 eV of the surface adventitious carbon. UV-vis diffused reflectance spectra of the samples studied were



Scheme 1. (a) Molecular structure of perylene-3,4,9,10-tetracarboxylic acid (PTCAD), (b) Schematic illustration for the formation of PTCAD/In₂O₃ porous NSs.

obtained for the dry-pressed disk samples using a UV-vis spectrometer (UV2550, Shimadzu, Japan). Photoluminescence was tested by F-280 fluorescence spectrophotometer. Electron Paramagnetic Resonance (EPR) Spectroscopy was acquired by Bruker E-500 spectrometer at 298 K.

2.5. Photoelectrochemical measurements

The linear sweep voltammograms (LSV) were carried out by using CHI 760D Instruments in a typical three-electrode system with the as-prepared powders coated on glassy carbon electrode as the working electrode, a Pt electrode as the counter electrode, and Hg/Hg₂Cl₂ (saturated KCl) electrode as the reference electrode. 1 M aqueous KOH solution was used as the electrolyte. Photocurrents were measured using the same instruments in a typical three-electrode system whose working electrode was changed to samples coated on ITO glass. 0.5 M aqueous Na₂SO₄ solution and 0.1 M KPi buffer was used as electrolyte, respectively, which were deaerated with high purity oxygen. Electrochemical impedance spectra (EIS) measurements used the same electrodes with photocurrents tests, and the frequency range was 1–10⁶ Hz with ac amplitude of 5 mV at 0.2 V under 300 W Xe lamp irradiation. The photocatalytic O₂ evolution experiments were carried out in a 200 mL Pyrex reactor sealed with silicone rubber septum at ambient temperature and atmospheric pressure coupled an online gas chromatograph (GC, TianMei company, GC-7900, Ar as the carrier gas) equipped with a thermal conductivity detector. A 300 W full gloss light (Beijing perfect science and Technology Co. Ltd.) was used as the light source. The photocatalyst (100 mg) were dispersed in a 100 mL 0.1 M AgNO₃ aqueous solution. Before irradiation, the system was vacuumed for 30 min in order to remove the dissolved air.

3. Results and discussion

3.1. Preparation and characterization of PTCAD/In₂O₃ NS

Xie et al. [31] have reported the fabrication of atoms-thick In₂O₃ porous sheets via a fast-heating strategy from the ultrathin cubic-In(OH)₃ sheets obtained through a mesoscopic-assembly of In-oleate complex. With similar preparation procedures, by mixing PTCAD (Scheme 1) with oleate ions, we prepared the porous PTCAD/In₂O₃ NS

from the in-situ PTCAD loaded In(OH)₃ NS. This method is adopted based on the hypothesis that first, PTCAD ions bearing functional COO-groups that may bond strongly with In³⁺ to form In-complexes as oleate ions did, meanwhile do not interrupt the inherent 2D structure constructed by the assembled oleate ions; second, the formation of the coordination bonds between PTCAD and In₂O₃ is expected to deliver effective photoinduced charge injection as have been documented [26]. Last but not the least, PTCAD is robust with high thermal stability to stand the heating temperature used for the In(OH)₃ transformation. Experimental details and characterization data can be found in supporting information. Typically, sodium oleate mixed with a given amount of PTCAD ions were added into indium nitrate solution to form mutual coordinated In-complexes, and the solution was transferred to the reaction kettle and react at a series of temperature to form a lamellar structure and then decomposed at a high temperature to form PTCAD/In₂O₃ NS. PTCAD ions were loaded in the molar ratio of 0.2%, 0.5%, 1%, 10% (with respect to In³⁺, and marked as **0.2-PTCAD/In₂O₃**, **0.5-PTCAD/In₂O₃**, **1-PTCAD/In₂O₃**, **10-PTCAD/In₂O₃**, respectively) to inspect the effect of PTCAD on the structure and water oxidation performance of the In₂O₃ NS. It should be noted that as we have expected, according to TGA results (Fig. S1), sodium oleate is totally decomposed while PTCAD kept firmly well without decomposition at 400 °C. Hence, thermal decomposition was carried out at 400 °C for 3 min in air, by which PTCAD/In(OH)₃ NS transformed into porous PTCAD/In₂O₃ NS completely. As indicated in the XRD pattern (Fig. 1), the overall microstructure of the PTCAD/In(OH)₃ NS at low PTCAD-loading is identical to the ultrathin In(OH)₃ 2D sheets obtained from the uniform In-oleate complex. For In(OH)₃ NS with high PTCAD-containing, for example 10% (10-PTCAD/In(OH)₃), beyond the sharp diffraction peaks from the cubic-In(OH)₃ (JCPDS file no.76-1464) [31], a weak peak at $2\theta = 27.9^\circ$ emerged (Fig. 1a and S2), which is typically ascribed to the π -stacking of the PTCAD framework that indicates the presence of the PTCAD assembly. After fast heating at 400 °C for 3 min, PTCAD/In(OH)₃ transformed completely into PTCAD/In₂O₃, which can be identified from the indicative diffractions of In₂O₃ (JCPDS file no.88-2160) in the XRD patterns (Fig. 1b).

HRTEM shown in Fig. 2 and Fig. S3 clear demonstrate the porous 2D sheet-like morphology of the as-obtained nano-hybrids. The presence of PTCAD ions have no big influence on morphology of the 2D sheet, while the lattice fringe indicate minor modification on the microstructure

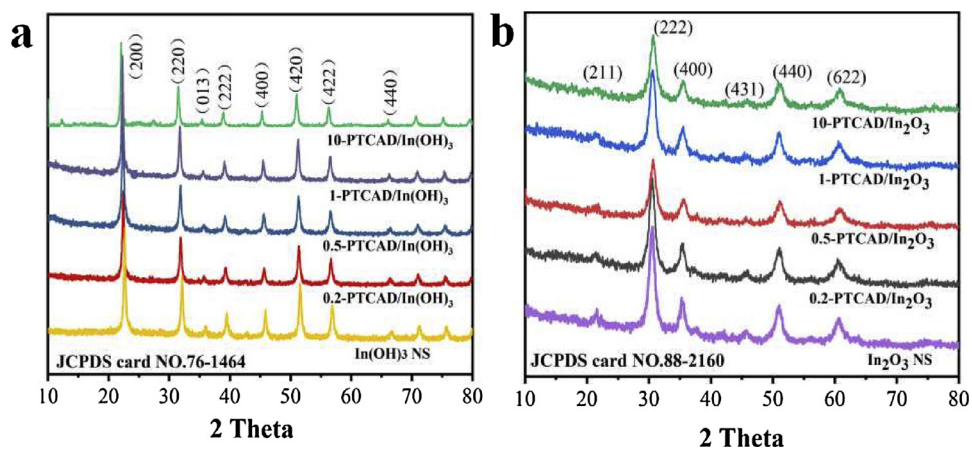


Fig. 1. XRD patterns of (a) PTCAD-In(OH)₃ NS, and (b) PTCAD-In₂O₃ NS.

compared to the In₂O₃ NS reported by Xie [10]. As exemplified by the HRTEM of the 0.5-PTCAD/In₂O₃ displayed in Fig. 2, other than the interplanar spacing of 0.293 nm referring to (222) facet, the lattice fringe spacing of 0.250 nm corresponding to (400) and (040) lattice spacing are distinguished explicitly, suggesting the presence of the polar {001} facets and matched well with the cubic structure of In₂O₃. Previous work [35,36] revealed that polar {001} facets are active in dissociation of the adsorbed H₂O molecules into H⁺ and OH⁻, meanwhile in favor of accumulating the positively charged holes, whereas nonpolar {111} facets are passivated. Accordingly, the PTCAD/In₂O₃ NS with much more exposed {001} facets is expected to be higher efficient for photoelectrochemical water splitting. However, when the

PTCAD content is increased to 10% (Fig. S4), lattice fringe from {001} facet disappeared and left only the lattice fringes from nonpolar {111} facets, which may indicate a depressed water splitting performance as will be disclosed hereinafter. Interestingly, at the absence of PTCAD, In₂O₃ slab along the [01-1] direction was obtained in Xie's work, which clearly demonstrates the effect of the organic molecules in control the orientation of crystal growth. The atomic force microscopy (AFM) images of PTCAD/In₂O₃ (Fig. S5) depict that the thickness of an individual nanosheet is about 2.30 nm to 2.50 nm, which is not greatly influenced by the concentration of PTCAD molecules. The Brunauer–Emmett–Teller (BET) surface area summarized in Table S1 and the pore volume (Fig. S6) showed that PTCAD/In₂O₃ NS possess relatively large

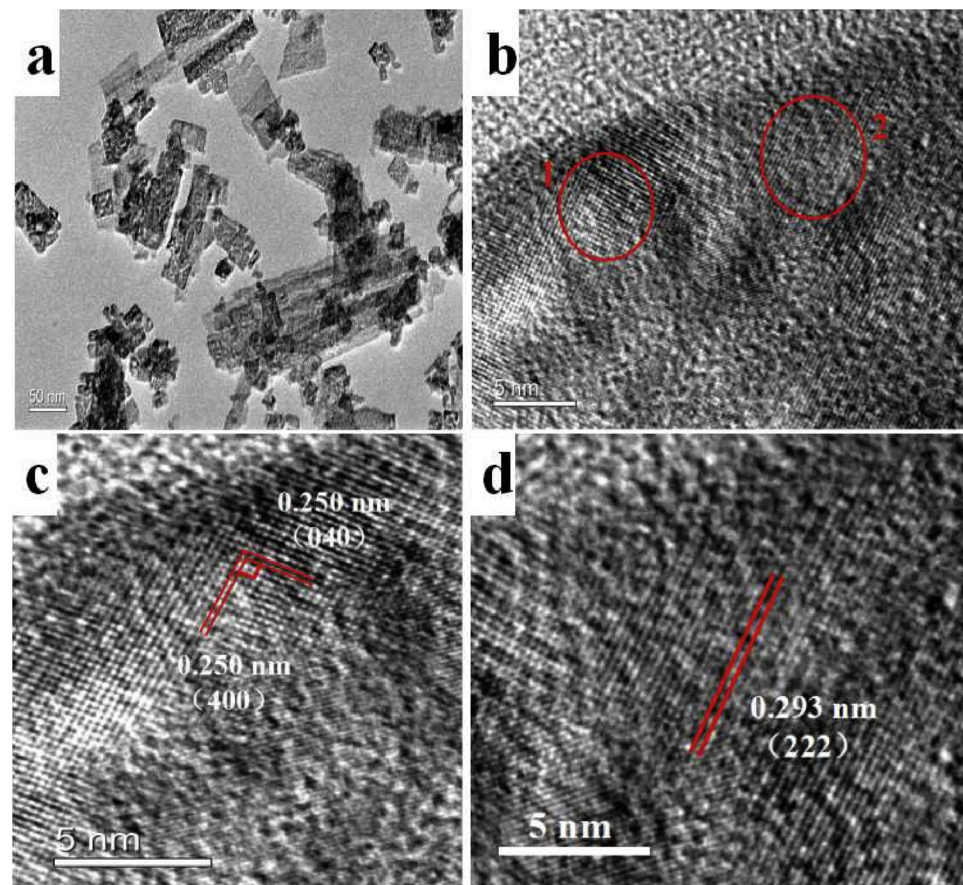


Fig. 2. TEM observation of (a) 0.5-PTCAD/In₂O₃ NS, and (b) lattice fringes of 0.5-PTCAD/In₂O₃ NS indicated by HRTEM. (c) and (d) are the amplified lattice fringes corresponding to 1 and 2 that noted in (b) respectively.

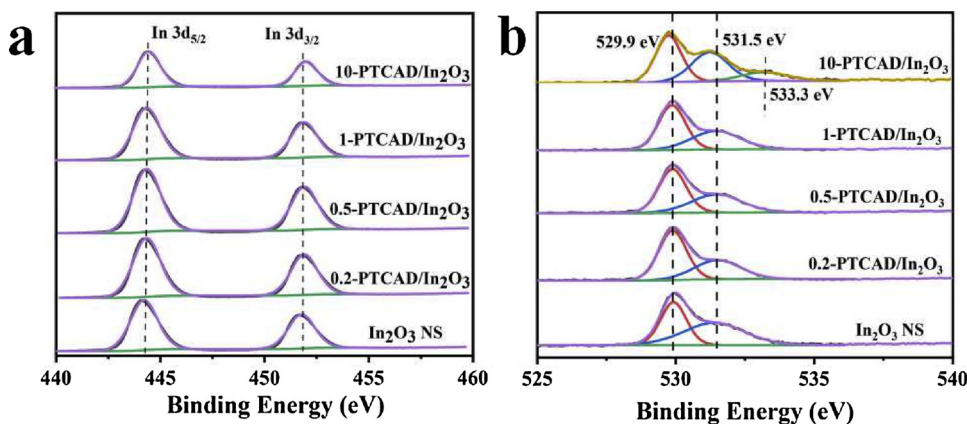


Fig. 3. XPS spectra of (a) In 3d core level, and (b) O 1s core level.

BET surface areas of around $90 \text{ m}^2 \text{ g}^{-1}$ superior to mostly reported inorganic or organic materials [9,22,37].

XPS was utilized to understand the overall chemical environment in the various PTCAD/In₂O₃ compositions. Fig. 3a displays the In 3d core level spectra of the PTCAD/In₂O₃ NS containing different amount of PTCAD with the pristine In₂O₃ NS. Two peaks at 444.2 and 451.7 eV are the spin-orbit split 3d_{5/2} and 3d_{3/2} of typical In(III), respectively [38]. Fig. 3b denotes the O 1s core level spectra. The peak at about 529.9 eV originates from the oxygen bond of In-O-In, and the peak at 531.5 eV tells the presence of the oxygen defects (O_v) [31,38,39]. A third peak at about 533.3 eV is found for 10-PTCAD/In₂O₃ NS, which could be ascribed to mass addition of PTCAD according to the O 1s core level spectra of PTCAD solid. The ratio of the area of O_v to that of the In-O-In region keeps consistence for all the PTCAD/In₂O₃ NS except for 10-PTCAD/In₂O₃ NS, which has the lowest O-vacancy concentration, indicating roughly the same O-vacancy concentrations regardless of the PTCAD concentration. It is well documented that the existence of a moderate number of oxygen vacancies could effectively reduce the BG by generation of new energy levels, and has a chance to improve the efficiency of solar energy utilization [38]. The BG reduction can be identified by absorption and photoluminescence spectra as will be disclosed hereinafter. Overall, the presence of PTCAD with low content has little effect on the morphology, BET, oxidation state, and O-vacancy of the In₂O₃ NS according to the above analysis. We therefore will focus on the charge injection behavior of PTCAD in the photo-driven WO performance hereinafter.

3.2. The energy level structure of PTCAD/In₂O₃ and inter-component charge transfer

The electronic effects on charge separation endowed by PTCAD coupling was investigated by UV-vis diffuse reflection spectra (DRS), Mott-Schottky (MS) measurements, X-ray photoemission spectroscopy (XPS) valence band spectra, and Electron spin-resonance spectroscopy (ESR) analysis. Fig. 4a depicted the UV-visible diffuse absorption spectra of all five samples containing diverse amount of PTCAD. Pristine In₂O₃ NS demonstrates strong absorption located mainly in the ultraviolet region with extension to visible areas due to the presence of O-vacancies. Upon hybridization with PTCADs, a broad absorption emerged in the visible region (from 500 to 800 nm), corresponding to the typical S₀-S₁ absorption of the perylene framework that could be figured out from the absorption spectra of the molecular PTCAD shown in Fig. S7 [40]. The refined structured cannot be identified, which may be the result of the π -aggregation of molecules at higher concentration as also indicated in XRD pattern. According to Tauc's relation [41], the band gap of each sample is estimated as shown in Fig. 4b. The BG of 0.2-PTCAD/In₂O₃ is approximately 2.16 eV which is close to that of the pristine In₂O₃ NS (2.20 eV), and is largely reduced compared with bulk

In₂O₃. Increasing of PTCAD content leads to remarkably narrowed BG which is in line with the more extended absorption in visible region. Specifically, the BG of 0.5-PTCAD/In₂O₃ is reduced to 2.02 eV, which is significant for making full use of the whole spectrum by stimulating electrons with lower-energy irradiation. It is worthy to mention that, though the overall absorption was extended largely to the visible region due to the presence of PTCAD, it may not necessarily reflect the substantial electron coupling between the two composites, which has always been overestimated in previous studies. Interactions between In₂O₃ and PTCAD, namely the band gap changes manipulated by PTCAD will be disclosed by electrochemical methods hereinafter.

The excitation-depended room-temperature photoluminescence spectra (PL) are provided in Fig. S8. Upon UV-light excitation, a broad emission from 350–550 nm was observed for PTCAD/In₂O₃ NSs with relative low PDI content (Fig. S8a), which was resulted mainly from the existence of singly ionized V_O [31,38,42]. The large red-shift of the emission peak compared to those of the reported V_O-rich In₂O₃ nanostructures may indicate the significantly narrowed BG due to the hybridization of PTCAD. 10-PTCAD/In₂O₃ showed dramatically different PL relative to all the other samples, where only a weak and unsymmetrical peak was observed at 350–400 nm, which may derived from the weak coupling between the PTCAD molecules in the H-aggregate formed within the hybrid [43]. This result was also consistent with the fact of the low V_O-containing in 10-PTCAD/In₂O₃. Noted that, emission from the pure PTCAD was not detected for 0.2, 0.5, and 1-PTCAD/In₂O₃, suggesting the fluorescence quenching occurred as the result of the photoexcited electron transfer from the PTCAD to In₂O₃. Such electron transfer can be better certified from the PL spectra obtained upon visible-light excitation. When excited at 500 nm, where PTCAD was excited but In₂O₃ was not (according to the absorption spectra), emissions from PTCAD were not observed (Fig. S8c), which should also be the consequence of the excited state quenching by In₂O₃.

The band alignments and the subsequent electron transfer process indicated above can be determined by the XPS analysis and Mott-Schottky (MS) plots. The valence band XPS spectra of all the hybrids (Fig. 4c and Fig. S9) displayed a constant value of 2.34 eV, despite the fact that the VB of the PTCAD solid is 1.65 eV. This may suggest that there is no interaction between PTCAD and In₂O₃ in the ground state. The bottom of conduction band (CB) for In₂O₃ NS, PTCAD/In₂O₃, and pure PTCAD can be estimated by the Mott-Schottky plots (Fig. 4d and S10). As shown in Fig. S10, The sign of the slope indicates the majority carrier is an n-type donor of all the measured samples. The flat-band potential (V_{fb}) of the PTCAD/In₂O₃ NS changes depending on the loadings of PTCAD. 0.2-PTCAD/In₂O₃ and 0.5-PTCAD/In₂O₃ have positively shifted potentials relative to that of the In₂O₃ NS, while high molar ratios loadings of PTCAD leads to negatively shifted potentials, indicating that the energy band structure at the surface is dependent upon PTCAD concentration. Taken the 0.5-PTCAD/In₂O₃ as an

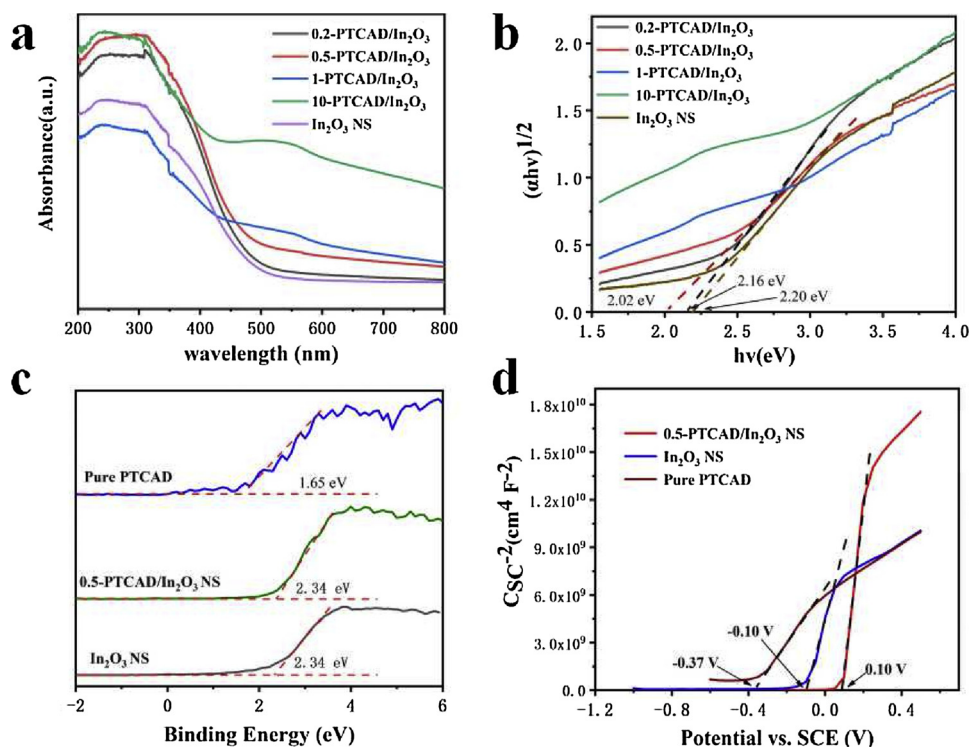


Fig. 4. (a, b) The UV-vis diffuse reflection spectra (DRS) of In₂O₃ NS, 0.2-PTCAD/In₂O₃, 0.5-PTCAD/In₂O₃, 1-PTCAD/In₂O₃, 10-PTCAD/In₂O₃; (c) The XPS valence band spectra and (d) Mott-Schottky plots of pure PTCAD, In₂O₃ NS, and 0.5-PTCAD/In₂O₃ NS.

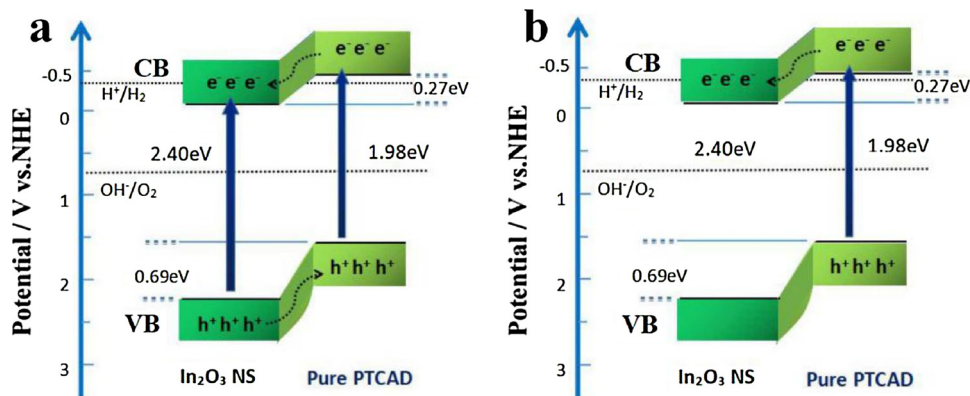
example, as shown in Fig. 4d, the V_{fb} for In₂O₃ NS, 0.5-PTCAD/In₂O₃, and pure PTCAD were -0.10 V, 0.10 V and -0.37 V vs. SCE (pH = 7), respectively. For n-type semiconductors, the bottom of CB is approximate 0.2 V higher than that of Fermi level [44]. Therefore, the CB at normal hydrogen electrode (NHE, pH = 7) can be calculated according to the following equation:

$$E_{CB} (\text{NHE, pH} = 7) = E_{fb} (\text{SCE, pH} = 7) + 0.24 - 0.2 \quad [37]$$

Therefore, the CB position of In₂O₃, 0.5-PTCAD/In₂O₃, and bulk PTCAD were estimated to be about -0.06 V, 0.14 V and -0.33 V vs. NHE, respectively. According to the position of CB and VB above mentioned, the BG of In₂O₃ NS, 0.5-PTCAD/In₂O₃, and bulk PTCAD were 2.40 eV, 2.20 eV and 1.98 eV, respectively. The BG of all the PTCAD/In₂O₃ NSs is calculated and provided in Table S2 and Fig. S11. The energy diagram of pure PTCAD and In₂O₃ NS reveals a large thermodynamic driving force for electron injection from the photoexcited PTCAD* into the CB of In₂O₃ NS. Apparently, loading of PTCAD has great contribution on CB but little influence on VB, suggesting strong electron coupling on CB. Density Functional Theory (DFT) calculations shows that electron deficient naphthalene diimide (NDI), PDI analogous, contributed to the CB of (Pb₂I₆)_n·(H₂DPNDI)_n·(H₂O)_n·(NMP) organic perovskite, inducing spatial electron-hole separation and therefore effective charge transfer between NDI and the Pb₂I₆ unit [44]. Here, similar behavior is expected for PTCAD and fast charge transfer is anticipated due to the large thermodynamic driving force and strong electron coupling between PTCAD and In₂O₃ NS. 0.5-PTCAD/In₂O₃ demonstrates distinctly narrowed BG relative to In₂O₃ NS, which coincides with the results obtained by UV-vis diffuse-reflectance spectrum (UV vis. DRS). However, further increase the amount of PTCAD leads to gradually increased BG, as the consequence of the lifted horizontal of CB, which is contrary to the broadened and enhanced absorption in DRS. In other words, overloaded PTCAD may not participate in orbital coupling at the molecular level. Nevertheless, based on the deduced energy levels of In₂O₃ NS and PTCAD, Type II band alignments [15] are formed as shown in Scheme 2. A directed charge carrier transfer under

light illumination can be inferred accordingly. Upon UV-light irradiation (Fig. 4a), charge carriers are generated in both PTCAD and In₂O₃, and then electrons transfer from the LUMO of PTCAD to the CB of In₂O₃, meanwhile holes will accumulate in the HOMO on PTCAD to realize charge separation. While under visible-light irradiation (> 500 nm) where In₂O₃ cannot be excited (Scheme 2b), electrons are excited from the HOMO of PTCAD and immigrate into In₂O₃, leaving the holes behind on PTCAD.

The above speculated charge transfer process was further verified by ESR analysis. As shown in Fig. S12a, under the shading condition, one Lorentzian line centered at a g value of 2.0020 was observed for PTCAD, which is the typical sign of free radicals generally observed for organic molecules. The intensity of this signal increased upon visible light irradiation, indicating the generation of more radicals by photo-induced intramolecular electron transition. This signal was also observed for all PTCAD/In₂O₃ hybrids as shown in Fig. 5a, and the intensity increased with the content of PTCDA. The g value has a slight shift, which may associate to the effects from the oxygen free radicals (oxygen vacancies) located in In₂O₃ sheets. Interestingly, as displayed in Fig. 5b, this signal in PTCAD/In₂O₃ (taken 0.5-PTCAD/In₂O₃ as an example) attenuated gradually after selective photoexcitation on PTCAD with visible light. In order to reveal this phenomenon, the kinetics processes of PTCAD and 10-PTCAD/In₂O₃ were traced, where three processes could be identified as shown in Fig. S12b. Specifically, upon light irradiation, a sharp signal increase was indeed demonstrated, corresponding to the photo-generation of PTCAD anion radicals. Subsequently, with constant light irradiation, the intensity of the signal decreased gradually and suddenly dropped to a minimum value without light, suggesting a rapid electron transfer from excited PTCAD to In₂O₃, or electron capturing by oxygen defects in In₂O₃. Afterwards, the signal gradually returned to its starting level in the dark, which may be the result of back electron transfer considering the strong electron-withdrawing nature of PTCAD. Overall, hybridization of PTCAD with In₂O₃ will facilitate photoinduced charge separation, which can be demonstrated by the enhanced photocurrent as will be disclosed below.



Scheme 2. Energy alignment of In_2O_3 NS and PTCAD and estimated charge transfer irradiated by (a) UV-light irradiation and (b) visible-light irradiation.

3.3. Photoelectrocatalysis oxidation performance of PTCAD/ In_2O_3 NSs

Electrocatalytic OER activities were evaluated by steady-state linear sweep voltammetry (LSV) in O_2 -saturated 1 M KOH solution, using a standard three-electrode system with Pt as the counter electrode and an $\text{Hg}/\text{Hg}_2\text{Cl}_2$ reference electrode (1 mol KCl-filled). Fig. 6a shows the polarization curves for all the samples. It can be figured out that loading PTCAD widely reduced the onset potential (V_{onset}) for the OER, and the corresponding catalytic activity thus increases compared to In_2O_3 NS, and the 0.5-PTCAD/ In_2O_3 NS being the most active composition. The overpotential (η) for a current density of 10 mA cm^{-2} decreased from $\sim 1.55 \text{ V}$ ($\sim 2.78 \text{ V}$ vs RHE) of In_2O_3 NS to $\sim 0.67 \text{ V}$ ($\sim 1.90 \text{ V}$ vs RHE) of 0.5-PTCAD/ In_2O_3 NS. Meanwhile, the smallest Tafel slope down to 56 mV dec^{-1} , which is highly reduced compared to that of In_2O_3 NS (120 mV dec^{-1}), suggesting an acceleration of OER reaction rate (Fig. 6b). It is worth mention that η depends on several factors including the bandgap, shift of V_{fb} , recombination of photogenerated carriers, and activation energy for the surface reaction [45]. The significantly reduced η of 0.5-PTCAD/ In_2O_3 NS may be a joint contribution from the following aspects: the mainly exposed active $\{001\}$ facets in 0.5-PTCAD/ In_2O_3 NS demonstrated by HRTEM observation was conducive to reduce activation energy for the surface reaction; PTCAD in moderation promotes the separation of photo-generated electrons and holes so as to inhibit photo-induced charge recombination; the greatly reduced V_{onset} together with the positively shifted V_{fb} of 0.5-PTCAD/ In_2O_3 NS relative to that of In_2O_3 NS made a significant contribution to the reduction of overpotential. All of the above results clearly indicate that the OER activity can be enhanced by the formation of type-II PTCAD/ In_2O_3 composite, and η can be manipulated by the amount of PTCAD. Among them, 0.5-PTCAD/ In_2O_3 NS performs the best OER activity.

The above analysis on energy alignment and electrocatalytic OER

activities strongly suggest the substantial photo-driven OER capability of the PTCAD/ In_2O_3 hybrids, which can be demonstrated by photo-induced current density assessed hereby. The transient photocurrent responses were evaluated for several on-off cycles of solar irradiation in Na_2SO_4 solution (0.5 mol L^{-1}). Fig. 7a shows a comparison of the photocurrent-time ($I-t$) curves under intermittent solar irradiation without bias potential. All the samples including bare In_2O_3 NS has an apparently boosted photocurrent in response to solar illumination, and the on-off cycles of the photocurrent are reproducible. Particularly, all the PTCAD/ In_2O_3 composites demonstrate enhanced photocurrent compared with each single component, suggesting more efficient charge separation and transport under solar irradiation on account of the synergistic effect between PTCAD and In_2O_3 . 0.5-PTCAD/ In_2O_3 displayed the highest photocurrent, which is more than 5 times higher than that of the pristine In_2O_3 NS, due to the ultrafast interfacial electron transfer. This value is indeed higher than that of PMPDI blended TiO_2 or SnO_2 films [27], which may indicate more effective electron coupling between PTCAD and In_2O_3 on account of energy level matching and molecular bonding. More interestingly, unlike the sharp photoanodic spike and quickly attenuated current signal ubiquitously observed in TiO_2 , SnO_2 and WO_3 blends [27], the photocurrent generated by the neat In_2O_3 NS and all the PTCAD decorated PTCAD/ In_2O_3 NSs demonstrated steady signals without attenuation, which clearly indicate the fast charge transfer to the electrolyte in competition with recombination on account of the 2D-limited conducting channels.

Electrochemical impedance spectroscopy (EIS) was analyzed by the Vorotynsev theoretical model to further disclose the charge separation process and the influence of the PTCAD on the electronic properties of the composites [40,46,47]. Fig. 7b showed the EIS Nyquist plots of all the samples measured at a bias potential of 0.3 V. Two parts, the linear part and the impedance curve part are included in the EIS Nyquist plots. The linear part was related to mass transfer in the electrode/electrolyte

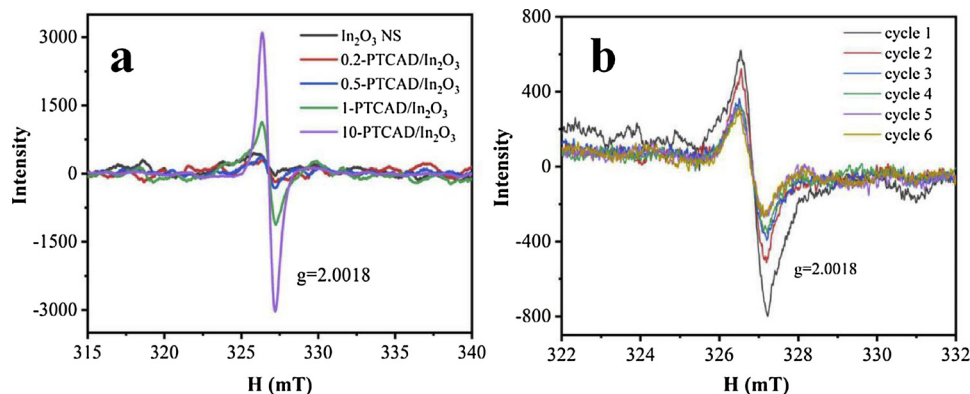


Fig. 5. ESR spectra of (a) PTCAD/ In_2O_3 NSs and (b) 0.5-PTCAD/ In_2O_3 upon visible light irradiation.

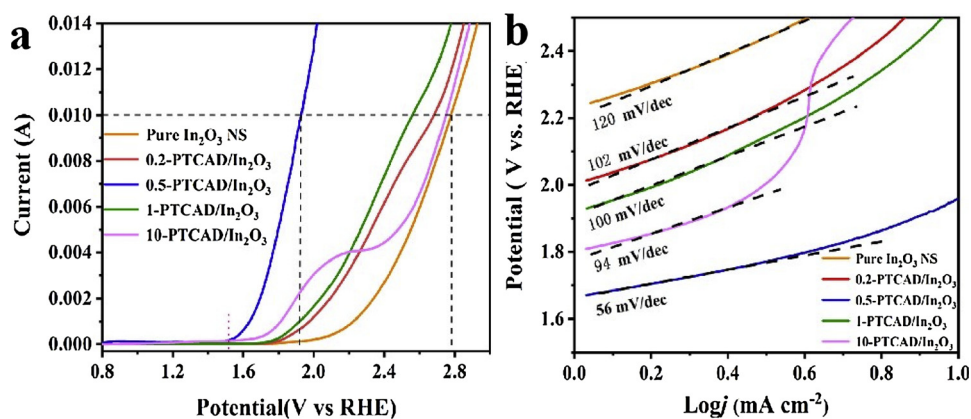


Fig. 6. (a) OER polarization curves, and (b) Tafel plots of PTCAD/In₂O₃ NS.

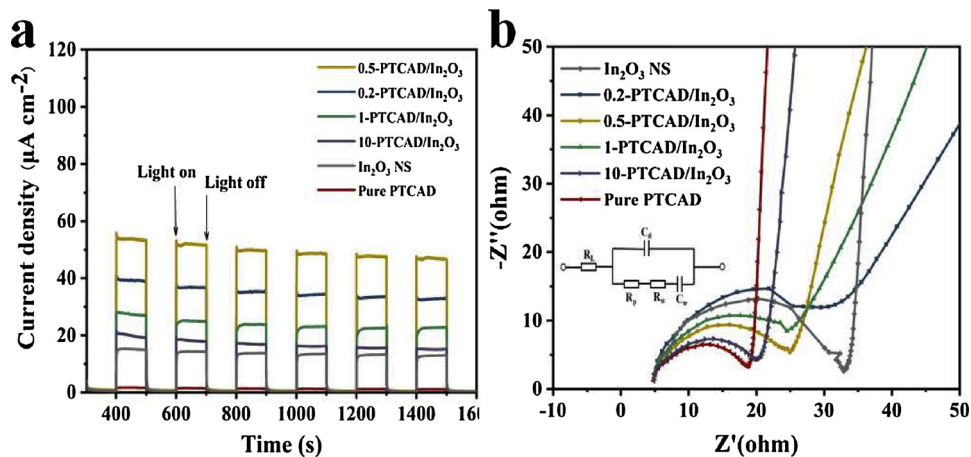


Fig. 7. (a) Transient photocurrent responses, and (b) Nyquist plots for PTCAD/In₂O₃ NS and the equivalent circles (inset) in Na₂SO₄ solution (0.5 mol L⁻¹).

interface, indicated that diffusion became dominant in the electrode process. A larger slope stands for a smaller diffusion coefficient [48]. The impedance curve part in the high-frequency region is an approximate semicircle, which indicates the complexity of the charge transfer process, the possible rate-determining step of the whole electrochemical reaction [49]. As shown in Fig. 7b, both the monomeric components PTCAD and In₂O₃ NS present the smallest diffusion coefficient in the linear part, namely the largest impedance of concentration polarization. For all the PTCAD/In₂O₃ hybrids, impedance of concentration polarization reduced with the dependence of the PTCAD content, suggesting that the addition of PTCAD facilitate electrolyte penetration and therefore the expected enhancement in reaction rate on the electrode interface. In the high frequency region, interestingly, solid PTCAD film has the smallest curvature radius while In₂O₃ NS has the largest one. This result is consistent with the slope obtained in the MS plots (Fig. S10), which indicates that carrier concentration on PTCAD (aggregates) is higher than that on the In₂O₃ NS, and might be the cause of the promoted charge transport. Indeed, the radii of the curves contracts along with increasing the PTCAD content, which is indicative of an accelerated kinetics of faradaic reaction profited from the PTCAD [48,49]. In short, the presence of the PTCAD works as a donor to promote the mass and charge transfer at the meantime, and finally leads efficient charge carrier transport and enhanced photocurrent density of the PTCAD/In₂O₃ NS hybrids. It has been elucidated that the doping amount of organic electron donor will control the balance of charge transfer and charge scattering in charge transport of In₂O₃ transistors [50]. Likewise, small amounts of PTCAD may dedicate a delicate balance between electron transfer and prefilling of immobile electron traps, which finally enhance charge transport. Large amounts of

dopants may create far more traps to be the charge recombination center. Considering the mass and charge transfer properties indicated in Fig. 7b, loading amount of PTCAD with 0.5 to 1 mole fraction is optimal. Specially, with the largely decreased BG, significantly reduced overpotential and fast and high photo-to-current responses, effective photo-driven OER performed on 0.5-PTCAD/In₂O₃ NS is anticipated.

PCET at semiconductor solution interfaces plays a pivotal role in photochemical water splitting. According to previous reports, phosphate buffer solutions (denoted as KPi buffer) could promote oxygen evolution due to its ability to accept and transfer protons produced in the PCET processes [51]. To evident the presence of PCET process, we checked the transient photocurrent response in KPi buffer (pH = 7, 0.1 mol L⁻¹) and compared with that obtained from Na₂SO₄ solution (pH = 7, 0.5 mol L⁻¹). As shown in Fig. 8, the current density of 0.5-PTCAD/In₂O₃ in KPi buffer reached about 100 μA cm⁻², which is 2 folds higher than that in Na₂SO₄ solution. The current density of pure In₂O₃ NS also enhanced in KPi buffer relative to that in Na₂SO₄ solution. The promotion in photocurrent in KPi buffer indicates the accelerated charge separation facilitated by protons, namely, PCET. More importantly, the presence of PTCAD highly promoted the PCET progress, which can be rationalized by a theoretical model provided in previous work [52]. It has been illuminated that for an organic radical TEMPO coupled ZnO nanocrystal, TEMPO· served as hydrogen atom acceptors from photoreduced ZnO nanocrystals to accomplish PCET [53]. In a similar way, multiple carboxyl containing PTCAD and its radical form (as demonstrated by EPR) provide rich proton exchange sites for tunneling protons from a surface oxygen of In₂O₃ NS, which results in more efficient PCET to promote water oxidation efficiency.

To demonstrate the effects of PTCAD on water oxidation,

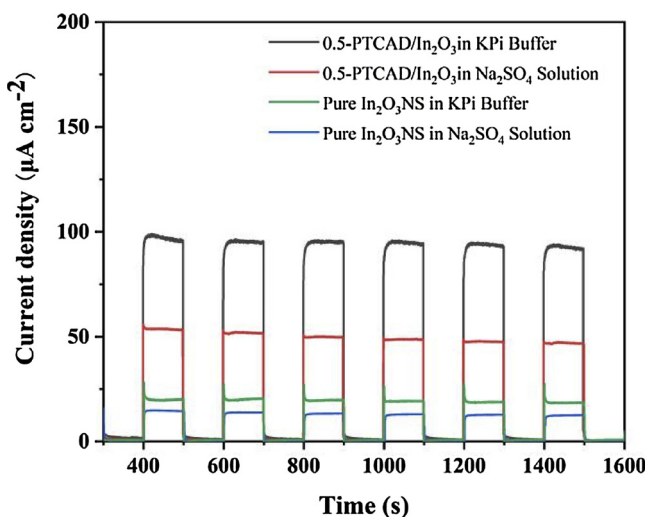


Fig. 8. Transient photocurrent responses in 0.1 M KPi buffer and 0.5 M Na₂SO₄ solution.

photocatalytic O₂ evolution activity of PTCDA coupled In₂O₃ hybrids was checked under simulated solar irradiation ($\lambda > 420$ nm) from an aqueous solution, and AgNO₃ was used as the sacrificial agent. As control, O₂ evolution of native In₂O₃ NS was also tested under the same condition. As shown in Fig. 9a, taken 0.5-PTCAD/In₂O₃ NS and 10-PTCAD/In₂O₃ NS as examples, the presence of PTCAD does contribute to promote the WO activity as can be found from the enhanced O₂ production per unit time than that of In₂O₃ NS. 0.5-PTCAD/In₂O₃ NS performed the highest photocatalytic activity, from which the O₂ yield reached 110 μmol g⁻¹ obtained within 8 h. Moreover, the oxygen evolution rate remains constant after 3 cycle tests (Fig. 9b), indicating the favorable stability of the hybrid catalysts.

Overall, PTCAD/In₂O₃ NSs, specifically the 0.5-PTCAD/In₂O₃ NS demonstrates features of robust broadband-light-driven photo-electrochemical water splitting performance on account of the strong electron coupling and synergistic effect between PTCAD and In₂O₃ NS. The mesopores In₂O₃ NS provides an unrivaled platform for fast interfacial charge transfer stemming from the extremely high surface percentage and quantum well effect. Bonding with PTCAD endowed further promoted photocatalytic efficiency in both the structural and electronic ways: first, implement the formation of the lattice plane that has higher activity in dissociation of H₂O into H⁺ and OH⁻; second, strong coupling with the CB of In₂O₃ NS to narrow the BG to enhance the broadband-excited charge generation; third, injecting the excited

electrons to CB of In₂O₃ NS meanwhile leaving holes behind to promote charge separation and decrease the overpotential; forth, benefiting the diffusion of charges and active species; last but not the least, PCET process endowed by PTCAD plays a key process to accelerate the surface photo-electrochemical reactions.

4. Conclusion

In summary, to check on the functionalization of OSC PDI derivatives in light-driven WO, an organic/inorganic composite, PTCAD/In₂O₃ NS, was fabricated via a rapid and facile method using PTCAD as mixed ligand. The porous PTCAD/In₂O₃ NSs indeed demonstrated further enhanced photocatalytic activity relative to the neat In₂O₃ NS, inheriting from both the structural and electronic effects on exerting PTCADs. Structurally, coordination of the organic PTCAD presented the ability to engineer the nanocrystals with more exposed active facets, which may significantly enhance oxygen production. From the perspective of electronic effects, type II alignment between PTCAD and In₂O₃ NS was formed, where PTCAD with large π -conjugated structure served as donor to smoothly inject the excited electron into the CB of In₂O₃ NS, leaving the photogenerated holes on VB of In₂O₃ NS that can transfer promptly to the HOMO of PTCAD to promote charge separation and decrease the overpotential. Specifically, 0.5-PTCAD/In₂O₃ NS demonstrated most promising broadband-light-driven WO activity, which may derive from its largely narrowed BG, significantly reduced overpotential, and fast and high photocurrent generation. The dependence of photocatalytic activity on the content of PTCAD disclosed the double-edged sword effect of PTCAD coupling. Namely, the content of the PTCAD has contrary influence on controlling both the lattice plane and charge separation process. Small amounts of PTCAD induced much more exposed active lattice face, meanwhile dedicated a delicate balance between electron transfer and prefilling of immobile electron traps to enhance charge transport. Excess amounts of PTCAD dopants lead to crystal surface passivation and may create far more traps to be the charge recombination center. Last but not the least, PCET, a key process for charge separation and water oxidation, exerts great influence in accelerating water oxidation, which is promoted markedly by PTCDA. The present studies have provided new insights to understand the coordination between organic and inorganic components and possibilities for photocatalytic enhancement.

Acknowledgement

Financial support from the National Natural Science Foundation of China (Grant 21371109) is gratefully acknowledged.

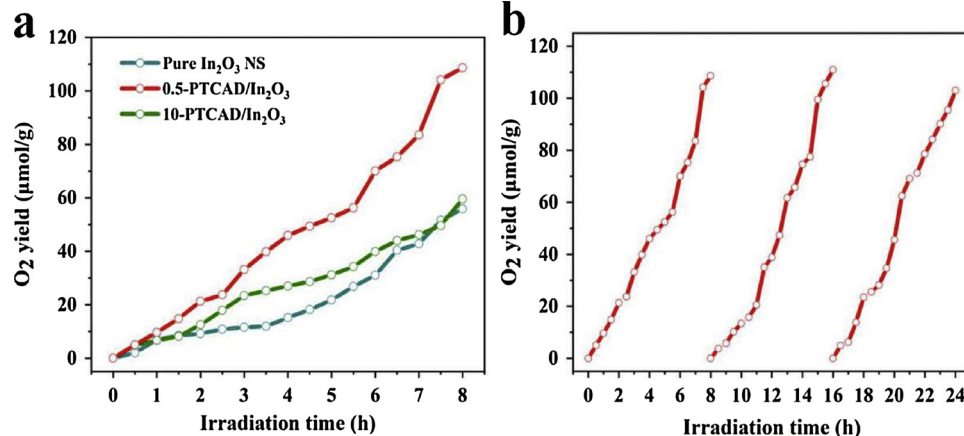


Fig. 9. (a) Photocatalytic O₂ evolution activities of pure In₂O₃ NS, 0.5-PTCAD/In₂O₃ NS and 10-PTCAD/In₂O₃ NS. (b) Plot of O₂ yield of 0.5-PTCAD/In₂O₃ NS during 3 cycles of repeated experiments.

Appendix A. Supplementary data

Supplementary material related to this article can be found, in the online version, at doi:<https://doi.org/10.1016/j.apcatb.2019.05.003>.

References

- [1] T.W. Woolerton, S. Sheard, Y.S. Chaudhary, F.A. Armstrong, Enzymes and bio-inspired electrocatalysts in solar fuel devices, *Energy Environ. Sci.* 5 (2012) 7470–7490.
- [2] J. Li, Z. Li, C. Ye, X. Li, F. Zhan, X. Fan, J. Li, B. Chen, Y. Tao, C. Tung, L. Wu, Visible light-induced photochemical oxygen evolution from water by 3,4,9,10-perylenetetracarboxylic dianhydride nanorods as an n-type organic semiconductor, *Catal. Sci. Technol.* 6 (2016) 672–676.
- [3] A. Fujishima, K. Honda, Electrochemical photolysis of water at a semiconductor, *Nature* 238 (1972) 37–38.
- [4] K.R. Reyes-Gil, Y. Sun, E. Reyes-García, D. Rafty, Characterization of photoactive centers in N-doped In_2O_3 visible photocatalysts for water oxidation, *J. Phys. Chem. C* 113 (28) (2009) 12558–12570.
- [5] B. You, N. Jiang, M. Sheng, S. Gul, J. Yano, Y. Sun, High-performance overall water splitting electrocatalysts derived from cobalt-based metal–organic frameworks, *Chem. Mater.* 27 (2015) 7636–7642.
- [6] R.D.L. Smith, M.S. Prévôt, R.D. Fagan, Z. Zhang, P.A. Sedach, M.K.J. Siu, S. Trudel, C.P. Berlinguet, Photochemical route for accessing amorphous metal oxide materials for water oxidation catalysis, *Science* 340 (2013) 60.
- [7] E.J. Popczun, C.G. Read, C.W. Roske, N.S. Lewis, R.E. Schaak, Highly active electrocatalysis of the hydrogen evolution reaction by cobalt phosphide nanoparticles, *Angew. Chem. Int. Ed.* 126 (2014) 5531–5534.
- [8] J. Wang, D.N. Tafen, J.P. Lewis, Z. Hong, A. Manivannan, M. Zhi, M. Li, N. Wu, Origin of photocatalytic activity of nitrogen-doped TiO_2 nanobelts, *J. Am. Chem. Soc.* 131 (2009) 12290–12297.
- [9] X. Gan, R. Zheng, T. Liu, J. Meng, R. Chen, X. Sun, X. Sun, N-Doped Mesoporous In_2O_3 for photocatalytic oxygen evolution from the In-based metal–organic frameworks, *Chem. Eur. J.* 23 (2017) 7264–7271.
- [10] E. Borgarello, J. Kiwi, M. Grätzel, E. Pelizzetti, M. Viscal, Visible light induced water cleavage in colloidal solutions of chromium-doped titanium dioxide particles, *J. Am. Chem. Soc.* 104 (1982) 2996–3002.
- [11] E.W. McFarland, H. Metiu, Catalysis by doped oxides, *Chem. Rev.* 113 (2013) 4391–4427.
- [12] X. Chang, T. Wang, P. Zhang, J. Zhang, A. Li, J. Gong, Enhanced surface reaction kinetics and charge separation of p–n heterojunction $\text{Co}_3\text{O}_4/\text{bivo}_4$ photoanodes, *J. Am. Chem. Soc.* 137 (2015) 8356–8359.
- [13] H. Li, Y. Zhou, W. Tu, J. Ye, Z. Zou, State-of-the-Art progress in diverse heterostructured photocatalysts toward promoting photocatalytic performance, *Adv. Funct. Mater.* 25 (2015) 998–1013.
- [14] A. Kudo, Y. Misaki, Heterogeneous photocatalyst materials for water splitting, *Chem. Soc. Rev.* 38 (2009) 253–278.
- [15] R. Marschall, Semiconductor composites: strategies for enhancing charge carrier separation to improve photocatalytic activity, *Adv. Funct. Mater.* 24 (2014) 2421–2440.
- [16] Motonori Watanabe, Dye-Sensitized Photocatalyst for effective water splitting catalyst, *Sci. Technol. Adv. Mater.* 18 (2017) 705–723.
- [17] W. Bi, X. Li, L. Zhang, T. Jin, L. Zhang, Q. Zhang, Y. Luo, C. Wu, Y. Xie, Molecular co-catalyst accelerating hole transfer for enhanced photocatalytic H_2 evolution, *Nat. Commun.* 6 (2015) 8647.
- [18] S. Hammes-Schiffer, Controlling electrons and protons through theory: molecular electrocatalysts to nanoparticles, *Acc. Chem. Res.* 51 (2018) 1975–1983.
- [19] V. Bulovid, P.E. Burrows, S.R. Forrest, J.A. Cronin, M.E. Thompson, Study of localized and extended excitons in 3,4,9,10-perylenetetracarboxylic dianhydride (PTCDA): spectroscopic properties of thin films and solutions, *Chem. Phys.* 210 (1996) 1–12.
- [20] C. Ye, J. Li, H. Wu, X. Li, B. Chen, C. Tung, L. Wu, Enhanced charge separation efficiency accelerates hydrogen evolution from water of carbon nitride and 3,4,9,10-perylene-tetracarboxylic dianhydride composite photocatalyst, *ACS Appl. Mater. Interfaces* 10 (2018) 3515–3521.
- [21] M. Pandey, G.M. Joshi, K. Deshmukh, N.N. Ghosh, N.A.N. Raj, Electrical conductivity, optical properties and mechanical stability of 3,4,9,10-perylenetetracarboxylic dianhydride based organic semiconductor, *J. Phys. Chem. Solids* 80 (2015) 52–61.
- [22] T. Sun, J. Song, J. Jia, X. Li, Xuan Sun, Real roles of perylenetetracarboxylic diimide for enhancing photocatalytic H_2 -production, *Nano Energy* 26 (2016) 83–89.
- [23] S. Ferrere, A. Zaban, B.A. Gregg, Dye sensitization of nanocrystalline tin oxide by perylene derivatives, *J. Phys. Chem. B* 101 (1997) 4490–4493.
- [24] J.T. Kirner, J.J. Stracke, B.A. Gregg, R.G. Finke, Visible-light-assisted photoelectrochemical water oxidation by thin films of a phosphonate-functionalized perylene diimide plus CoO_x cocatalyst, *ACS Appl. Mater. Interfaces* 6 (2014) 13367–13377.
- [25] F. Ronconi, Z. Syrigiannis, A. Bonasera, M. Prato, R. Argazzi, S. Caramori, V. Cristina, C.A. Bignozzi, Modification of nanocrystalline WO_3 with a dicationic perylene bisimide: applications to molecular level solar water splitting, *J. Am. Chem. Soc.* 137 (2015) 4630–4633.
- [26] J.T. Kirner, R.G. Finke, Sensitization of nanocrystalline metal oxides with a phosphonate-functionalized perylene diimide for photoelectrochemical water oxidation with a CoO_x catalyst, *ACS Appl. Mater. Interfaces* 9 (2017) 27625–27637.
- [27] R.J. Lindquist, B.T. Phelan, A. Reynal, E.A. Margulies, L.E. Shoer, J.R. Durrant, M.R. Wasielewski, Strongly oxidizing perylene-3,4-dicarboximides for use in water oxidation photoelectrochemical cells, *J. Mater. Chem. A* 4 (2016) 2880–2893.
- [28] B. Zhang, N. Zhang, J. Chen, Y. Hou, S. Yang, J. Guo, X. Yang, J. Zhong, H. Wang, P. Hu, H. Zhao, H. Yang, Turning indium oxide into a superior electrocatalyst: deterministic heteroatoms, *Sci. Rep.* 3 (2013) 3109.
- [29] C. Chen, J. Moir, N. Soheilnia, B. Mahler, L. Hoch, K. Liao, V. Hoepfner, P. Brien, C. Qian, L. He, G.A. Ozin, Morphology-controlled In_2O_3 nanostructures enhance the performance of photoelectrochemical water oxidation, *Nanoscale* 7 (2015) 3683–3693.
- [30] A. Walsh, J.L.F.D. Silva, S. Wei, C. Korber, A. Klein, L.F.J. Piper, A. DeMasi, K.E. Smith, G. Panaccione, P. Torelli, D.J. Payne, A. Bourlange, R.G. Egdel, Nature of the band gap of In_2O_3 revealed by first-principles calculations and X-ray spectroscopy, *Phys. Rev. Lett.* 100 (2008) 167402.
- [31] F. Lei, Y. Sun, K. Liu, S. Gao, L. Liang, B. Pan, Y. Xie, Oxygen vacancies confined in ultrathin indium oxide porous sheets for promoted visible-light water splitting, *J. Am. Chem. Soc.* 136 (2014) 6826–6829.
- [32] Y.F. Sun, S. Gao, F.C. Lei, Y. Xie, Atomically-thin two-dimensional sheets for understanding active sites in catalysis, *Chem. Soc. Rev.* 44 (2015) 623–636.
- [33] X. Huang, Z.Y. Zeng, H. Zhang, Metal dichalcogenide nanosheets: preparation, properties and applications, *Chem. Soc. Rev.* 42 (2013) 1934–1946.
- [34] Y.F. Sun, S. Gao, F.C. Lei, C. Xiao, Y. Xie, Ultrathin Two-dimensional inorganic materials: new opportunities for solid state nanochemistry, *Acc. Chem. Res.* 48 (2015) 3–12.
- [35] M. Sun, S.J. Xiong, X.L. Wu, C.Y. He, T.H. Li, P.K. Chu, Enhanced photocatalytic oxygen evolution by crystal cutting, *Adv. Mater.* 25 (2013) 2035–2039.
- [36] M. Meng, X. Wu, X. Zhu, L. Yang, Z. Gan, X. Zhu, L. Liu, P.K. Chu, Cubic In_2O_3 microparticles for efficient photoelectrochemical oxygen evolution, *J. Phys. Chem. Lett.* 5 (2014) 4298–4304.
- [37] J. Wang, W. Shi, D. Liu, Z. Zhang, Y. Zhu, D. Wan, Supramolecular organic nanofibers with highly efficient and stable visible light photooxidation performance, *Appl. Catal. B: Environ.* 202 (2017) 289–297.
- [38] J. Gan, X. Lu, J. Wu, S. Xie, T. Zhai, M. Yu, Z. Zhang, Y. Mao, S.C.I. Wang, Y. Shen, Y. Tong, Oxygen vacancies promoting photoelectrochemical performance of In_2O_3 nanocubes, *Sci. Rep.* 3 (2013) 1021.
- [39] B. Li, Y. Xie, M. Jing, G. Rong, Y. Tang, G. Zhang, In_2O_3 hollow microspheres: synthesis from designed $\text{In}(\text{OH})_3$ precursors and applications in gas sensors and photocatalysis, *Langmuir* 22 (2006) 9380–9385.
- [40] W. Wei, D. Liu, Z. Wei, Y. Zhu, Short-range $\pi-\pi$ stacking assembly on p25 TiO_2 nanoparticles for enhanced visible-light photocatalysis, *ACS Catal.* 7 (2017) 652–663.
- [41] J. Tauc, R. Grigorovici, A. Vancu, Optical properties and electronic structure of amorphous germanium, *Phys. Stat. Sol.* 15 (2) (1966) 627–637.
- [42] F. Gu, C. Li, D. Han, Z. Wang, Manipulating the defect structure (V_0) of In_2O_3 nanoparticles for enhancement of formaldehyde detection, *ACS Appl. Mater. Interfaces* 10 (2018) 933–942.
- [43] N.J. Hestand, F.C. Spano, Expanded theory of H-and J-molecular aggregates: the effects of vibronic coupling and intermolecular charge transfer, *Chem. Rev.* 118 (2018) 7069–7163.
- [44] C.N. Savory, R.G. Palgrave, H. Bronstein, D.O. Scanlon, Spatial electron-hole separation in a one dimensional hybrid organic-inorganic lead iodide, *Sci. Rep.* 6 (2016) 20626.
- [45] L. Xi, K.M. Lange, Surface modification of hematite photoanodes for improvement of photoelectrochemical performance, *Catal. Today* 8 (2018) 497.
- [46] M.A. Vorotyntsev, L.I. Daikhin, M.D. Levi, Modelling the impedance properties of electrodes coated with electroactive polymer films, *J. Electroanal. Chem.* 364 (1994) 37–49.
- [47] M. Mohamadi, D. Takahashi, T. Itoh, I. Uchida, Electrochemical stability of thin film limn_2O_4 cathode in organic electrolyte solutions with different compositions at 55°C, *Electrochim. Acta* 47 (2002) 3483–3489.
- [48] F. Mansfeld, Use of electrochemical impedance spectroscopy for the study of corrosion protection by polymer coatings, *J. Appl. Electrochem.* 25 (1995) 187–202.
- [49] J. Bobacka, A. Lewenstam, A. Ivaska, Electrochemical impedance spectroscopy of oxidized poly(3,4-ethylenedioxythiophene) film electrodes in aqueous solutions, *J. Electroanal. Chem.* 489 (2000) 17–27.
- [50] W. Huang, L. Zeng, X. Yu, P. Guo, B. Wang, Q. Ma, R.P.H. Chang, J. Yu, M.J. Bedzyk, T.J. Marks, A. Facchetti, Metal oxide transistors via polyethylenimine doping of the channel layer: interplay of doping, microstructure, and charge transport, *Adv. Funct. Mater.* 26 (2016) 6179–6187.
- [51] B. Ni, K. Wang, T. He, Y. Gong, L. Gu, J. Zhuang, X. Wang, Mimic the photosystem II for water oxidation in neutral solution: A case of Co_3O_4 , *Adv. Electron. Mater.* 8 (2018) 1702313.
- [52] S. Ghosh, J. Castillo-Lora, A.V. Soudackov, J.M. Mayer, S.H. Schiffer, Theoretical insights into proton-coupled electron transfer from a photoreduced ZnO nanocrystal to an organic radical, *Nano Lett.* 17 (2017) 5762–5767.
- [53] J.N. Schrauben, R. Hayoun, C.N. Valdez, M. Braten, L. Fridley, J.M. Mayer, Titanium and zinc oxide nanoparticles are proton-coupled electron transfer agents, *Science* 336 (2012) 1298–1301.